



HAL
open science

Uranium speciation control by uranyl sulfate and phosphate in tailings subject to a Sahelian climate, Cominak, Niger

Florian Lahrouch, Benoit Baptiste, Kathy Dardenne, Jörg Rothe, Erik Elkaim, Michael Descostes, Martine Gerard

► To cite this version:

Florian Lahrouch, Benoit Baptiste, Kathy Dardenne, Jörg Rothe, Erik Elkaim, et al.. Uranium speciation control by uranyl sulfate and phosphate in tailings subject to a Sahelian climate, Cominak, Niger. *Chemosphere*, 2022, 287, pp.132139. 10.1016/j.chemosphere.2021.132139 . hal-03963752

HAL Id: hal-03963752

<https://hal.science/hal-03963752>

Submitted on 16 Oct 2023

HAL is a multi-disciplinary open access archive for the deposit and dissemination of scientific research documents, whether they are published or not. The documents may come from teaching and research institutions in France or abroad, or from public or private research centers.

L'archive ouverte pluridisciplinaire **HAL**, est destinée au dépôt et à la diffusion de documents scientifiques de niveau recherche, publiés ou non, émanant des établissements d'enseignement et de recherche français ou étrangers, des laboratoires publics ou privés.



Distributed under a Creative Commons Attribution - NonCommercial 4.0 International License

1 Uranium speciation control by uranyl sulfate and phosphate in tailings
2 subject to a Sahelian climate, Cominak, Niger.

3 Florian Lahrouch^{1*}, Benoit Baptiste¹, Kathy Dardenne², Jörg Rothe², Erik Elkaim³, Michael
4 Descostes^{4,5}, and Martine Gerard^{1*}

5 ¹ *Sorbonne Université, CNRS UMR7590, MNHN, IRD, Institut de minéralogie, de physique
6 des matériaux et de cosmochimie (IMPMC), 4 place Jussieu, F- 75005, Paris, France*

7 ² *Karlsruhe Institute of Technology, Institute for Nuclear Waste Disposal (INE), P.O. Box
8 3640, D-76021 Karlsruhe, Germany*

9 ³ *Synchrotron SOLEIL, L'Orme des Merisiers, Saint-Aubin, BP 48, F-91192 Gif-sur-Yvette
10 Cedex, France*

11 ⁴ *ORANO Mines, Environmental R & D Department, 125 avenue de Paris, F-93320,
12 Châtillon, France*

13 ⁵ *Centre de Géosciences, MINES ParisTech, PSL University. 35 rue St Honoré, 77300
14 Fontainebleau, France*

15

16 **Highlights:**

17

- 18 • Sulfate and phosphate groups control U mobility in the tailings environment
- 19 • Neoformation of uranyl sulfates is favored by evapotranspiration phenomena
- 20 • Uranyl phosphate minerals are efficient traps for uranium long-term mobility
- 21 • Inherited U(IV) phases included in quartz are identified in tailings

22

23 **Keywords**

24 Uranium, Mining wastes, Uranium migration, EXAFS spectroscopy, Environment, uranyl
25 phosphate, uranyl sulfate

26 **Abstract**

27

28 Long-term uranium mobility in tailings is an environmental management issue. The present
29 study focuses on two U-enriched layers, surficial and buried 14.5 m, of the tailings pile of
30 Cominak, Niger. The acidic and oxidizing conditions of the tailings pile combined with
31 evapotranspiration cycles related to the Sahelian climate control U speciation. Uraninite,
32 brannerite, and moluranite as well as uranophane are relict U phases. EXAFS spectroscopy,
33 HR-XRD, and SEM/WDS highlight the major role of uranyl sulfate groups in uranium
34 speciation. Uranyl phosphate neoformation in the buried layer (paleolayer) acts as an efficient
35 trap for uranium.

36

37 **Introduction**

38 Tailing management related to uranium mining activity raises environmental concern among
39 governmental authorities and mining companies regarding the long-term mobility of
40 radioactive elements. The tailings generated by uranium extraction consist of residual ore
41 minerals. The uranium extraction yield generally around 95% related to the milling process
42 and ore mineralogy (Chautard et al., 2020), and by consequence, the uranium concentration in
43 the tailings is rather low. The residual uranium still present in the tailings, composed of U-
44 238, U-235 and U-234 (half-lives of 4.5 billion years, 703 million years and 245 thousand
45 years, respectively), is a possible source of radioactive contamination. The long-term
46 management of a large quantity of U-tailings, approximately 2 billion tons in the world
47 (Steinhausler and Zaitseva, 2007), remains an environmental management issue. However,
48 nearly 50% of the current world U production is accomplished preferentially by in situ
49 recovery (ISR), 31435 tons produced in 2019 (WNA, 2019), and does not produce equivalent
50 tailings configurations. The radioactive descendants of U, representing 80% of the total initial
51 radioactivity of the ore, are still present in the tailings (Abdelouas, 2006). Among these
52 radionuclides, Ra-226 (half-life of 1600 years) is particularly studied because of its high
53 specific activity ($3.66 \cdot 10^{10} \text{ Bq}\cdot\text{g}^{-1}$) (Nirdosh et al., 1984, Molinari et al., 1990, Fesenko et al.,
54 2014, Besançon et al., 2020) which leads to the continuous production of Rn-222 known for
55 its radiotoxicity (Martin and Tuck, 1959; King et al., 1982). Most of the tailings are stored as
56 piles close to the mining plants or disposed of by backfilling former uranium mines. Usually,
57 once mining operations cease, tailings are protected by waste rocks or water cover, which
58 form a radiological barrier against the emission of Rn-222, a radioactive gas descendant of
59 Ra-226 (Roberston et al., 2019, Ballini et al., 2020; Chautard et al., 2020). The chemical and
60 mechanical process of extracting uranium results in a reactive tailing environment containing
61 residual and oxidized ores and chemical reagents such as sulfuric and nitric acid or lime, in

62 the case of neutralization. In any case, the tailings evolve through a large variety of
63 precipitation/dissolution processes controlling uranium migration.

64 The residual uranium found in the tailings comes from refractory uranium phases such as
65 monazite ($\text{REE-U}^{\text{IV}}\text{PO}_4$) and brannerite ($\text{U}^{\text{IV}}\text{-Ti}_2\text{O}_6$) or from coffinite ($\text{U}^{\text{IV}}(\text{SiO}_4)_{1-x}(\text{OH})_{4x}$)
66 and uraninite ($\text{U}^{\text{IV}}\text{O}_2$) when entrapped in quartz, feldspar, or mica, which inhibit their
67 reactivity (Boekhout et al., 2015; Ballini et al., 2020; Chautard et al., 2020). However, if
68 coffinite and uraninite grains are directly exposed to oxidizing conditions, these U(IV)
69 minerals will oxidize with time into soluble uranyl groups ($[\text{U}^{\text{VI}}\text{O}_2]^{2+}$) that are known to be
70 mobile (Grenthe et al., 2006). Under natural conditions, secondary minerals such as
71 phyllosilicates, ferric oxyhydroxides or phosphates, generated by the weathering of primary
72 rocks, control uranium migration through different processes, such as sorption or precipitation
73 (Jin et al., 2016; Cretaz et al., 2013; Lee et al., 2011; Tayal et al., 2019; Lahrouch et al. 2021).
74 In the tailings, secondary mineral neof ormation depends on the nature of the ore parent rock,
75 the chemical reagents used in the extraction or neutralization processes and the storage
76 method. Therefore, gypsum and calcite formation are commonly observed in tailings due to
77 the high concentrations of sulfates, calcium and carbonates related to the ore process
78 (Jamieson, 2011; Lin et al., 2018). Uranyl (UO_2^{2+}) forms soluble complexes with a variety of
79 anionic species, including sulfate, phosphate or carbonate, which tend to limit its hydrolysis
80 and increase its mobility (Langmuir, 1978, Singh et al., 2010). The low solubility of uranyl
81 phosphate complexes generally reduces uranium mobility. Conversely, sorption on mineral
82 phases such as ferric oxyhydroxides or precipitation of secondary minerals such as uranyl
83 phosphates tend to limit U mobility (His and Langmuir, 1985; Murakami et al., 2017).

84 Low pH and sulfate enrichment are commonly described in acid mine drainage (AMD) to
85 favor the metal migration (Johnson and Hallberg, 2005; Morin and Calas, 2006; Park et al.,

86 2019), including uranium (Evangelou et al., 1995; Edwards et al., 2000). Such an acidic rich
87 sulfate environment is also reported in U-tailings, which are leached by sulfuric acid and not
88 neutralized before their deposition (Carvalho et al., 2005; Déjeant et al., 2016). The sulfate
89 groups form stable complexes with uranyl, whether in acidic conditions with the formation of
90 binary uranyl sulfate complexes or at low to near-neutral pH conditions, which favor the
91 formation of ternary uranyl hydroxosulfate complexes (Cox et al., 1989; Grenthe et al., 1992;
92 Grenthe et al., 1993; Shock et al., 1997). Most uranyl sulfate complexes are soluble in dilute
93 groundwaters and precipitate where evaporation is significant to form uranyl sulfate minerals
94 (Finch and Murakami 1999). Hence, the occurrence of uranyl sulfate minerals was observed
95 under underground alteration conditions, both in weathering mining dumps (Krivovichev and
96 Plàsil, 2013) and in mill-tailings (Schindler et al., 2012). Uranopilite formation,
97 $(\text{UO}_2)_6\text{SO}_4\text{O}_2(\text{OH})_6 \cdot (\text{H}_2\text{O})_8$ occurs early in the alteration process of the primary U^{IV} phases
98 involving acidic S-rich solution (Burns, 2001). This hydrated uranyl sulfate is easily
99 hydrolyzed or dissolved and has a high U/S ratio. Moreover, uranopilite turns into meta-
100 uranopilite after dehydration (Krivovichev and Plàsil, 2013). Zippeite group minerals are
101 hydrated uranyl sulfates $\text{M}(\text{UO}_2)_4(\text{SO}_4)_2\text{O}_2(\text{OH})_2 \cdot (\text{H}_2\text{O})_4$, containing monovalent (K^+ , Na^+ ,
102 NH_4^+), divalent (Mg^{2+} , Zn^{2+} , Co^{2+} , Ni^{2+} , Cu^{2+} , Ca^{2+}), or trivalent (Y^{3+} , rare earth elements)
103 cations. The zippeite structure was identified as uranyl sulfate sheets with cations located in
104 the interlayer, such as Mg in octahedral coordination for magnesium zippeite (Brugger et al.
105 2003) or Na for natrozippeite (Sharifironizi and Burns, 2018).

106 Phosphates also play an important role in uranium migration. Indeed, like sulfates, phosphate
107 groups form strong complexes with uranyl ions. The uranyl phosphate complexes can be
108 sorbed on minerals such as ferrihydrite, which results in an increase in uranyl uptake on
109 ferrihydrite (Payne et al., 1996; Lahrouch et al. 2021). The rather low solubility of these
110 complexes leads to their precipitation as autunite or metatorbernite mineral groups (Cretaz et

111 al., 2013). Under acidic conditions and depending on the ratio of carbonate to phosphate in
112 the system, the solubility of uranyl phosphate complexes is lower than that of uranyl
113 oxyhydroxides (Felmy et al., 2005; Grenthe and Konings, 1992; Langmuir, 1978; Rai et al.,
114 2005). The formed uranyl phosphate minerals are relatively insensitive to the system redox
115 potential and are also more resistant to dissolution than other uranium minerals, such as
116 uraninite, under oxic conditions outside of their stability fields (Campbell et al., 2011; Sowder
117 et al., 2001; Wellman, 2006; Wellman et al., 2009). Therefore, the precipitation of uranyl
118 phosphates, dominated in the environmental systems by autunite and meta-autunite formation,
119 prevents uranium mobility and holds uranium concentrations in groundwater rather low
120 (Murakami et al., 1997, 2005; Jensen et al., 2002; Jerden et al., 2003; Denecke et al., 2005;
121 Jerden and Sinha, 2003, 2006;).

122 In the present study, we investigate the evolution of uranium-bearing phases in tailings from
123 the COMINAK mine, Niger. Desert and subtropical weathering (Dodo and Zuppi, 1999)
124 favor the formation of sulfate species through strong evaporation phenomena (Finch and
125 Murakami 1999). Previous results indicate local reconcentrations of U up to several thousand
126 ppm within the tailings pile through oxidation and reprecipitation reactions associated with
127 uranyl sulfate and phosphate occurrences (Déjeant et al., 2014 and 2016; Angileri et al.,
128 2018). In this paper, we present a thorough characterization of most U-enriched layers in the
129 tailings pile, including both bulk and in situ characterizations. Extent X-ray Absorption to
130 Fine Structure spectroscopy (EXAFS) and High Resolution X-Ray Diffraction (HR-XRD)
131 were performed on powder samples to identify the dominant uranium species and
132 parageneses. Space-resolved EXAFS spectroscopy and Wavelength Dispersive Spectroscopy
133 (WDS) microprobe analyses on petrographic thin sections made it possible to identify
134 neoformed uranyl sulfates and uranyl phosphates. Based on these valuable data, the
135 occurrence of uranium-bearing phases related to the formation conditions as well as long-term

136 uranium retention in the postmining environment will be discussed.

137 **Materials and Methods**

138

139 *Mining site description and associated sampling*

140 The COMINAK mine opened in 1978 and produced approximately 2000 t U/year. The
141 stratiform roll front-type deposit formed in lower Carboniferous Guezouman sandstones
142 (quartz grains associated with feldspar and clay minerals). Most of the uranium occurrence is
143 attributed to volcanic activity but to a lesser extent from erosion and leaching of the
144 crystalline basement of the Air crystalline basement. Primary U-bearing phases are composed
145 of micrometric uraninite and coffinite. Minor U refractory minerals are micrometric U–Ti and
146 U–Mo oxides (Forbes, 1989; Pagel et al., 2005; Cavellec, 2006; Dejeant et al. 2014, 2016).
147 The ore grade is approximately 4000 ppm but shows variation with time (~3000–5000 ppm).
148 Ore processing is based on acidic and oxidizing dissolution. The ore is first crushed, then
149 oxidized and leached with acid. This process liberates microphases of U associated with
150 gangue and solubilizes U. The leaching operation is performed simultaneously with sulfuric
151 acid and minor nitric acid. After flocculation using guar gum, the solid fraction (i.e., the mill
152 tailings) is washed, and the U-rich pulp is filtered. The process efficiency is approximately
153 90–96%; thus, some residual U remains in the tailings after this step. Dissolved U is then
154 stripped of the pregnant liquor using liquid solvents. U is finally recovered as MgU₂O₇ (s)
155 (yellow cake). The tailings of COMINAK are not neutralized with lime and are therefore
156 acidic. The pH of pore waters was determined to be less than 4.

157

158 This pile, containing approximately 22 million tons of tailings, is located in the Sahel Desert,
159 where the climate is extremely arid with an annual mean temperature of 31 °C and annual

160 precipitation of approximately 40 mm (Dodo and Zuppi, 1999). During deposition, fresh
161 tailings are irrigated with mine water to reduce dust dispersion and improve the flow down
162 the slopes of the pile. Strong evaporation phenomena occur, leading to the formation of a
163 hardened crust (hard pan) at the surface of the pile.

164 Tailing samples containing high uranium concentrations were selected for this study (Déjeant
165 et al., 2014; 2016). V126 and C11-14,5 were collected at the surface of the tailings pile and at
166 14.5 m depth in a former surface crust that has been buried over the years of activities
167 (namely, paleolayer). Their uranium concentration is equal to 4100 ppm for V126 and 2250
168 ppm for C11-14,5, suggesting a strong U reconcentration.

169

170 *Scanning electronic microscopy (SEM) and wavelength-dispersive X-ray (WDS)*
171 *spectroscopy* microprobe.

172 SEM images using backscattering electron mode (BSE) were recorded at 15, 20, and 25 keV
173 on a ZEISS Supra 55 VP (ECCE TERRA, Observatoire des Sciences de l'Univers, Sorbonne
174 University -INSU). WDS microprobe characterizations were achieved for Al, Ba, Ca, Fe, K,
175 Mg, Mn, Mo, Na, P, S, Si, Th, Ti, V, Zr, Zn and U with a CAMECA SX-FIVE equipped with
176 five WDS and one EDS detector (CAMPARIS ECCE TERRA, Sorbonne University). The
177 spatial resolution was set at $1\mu\text{m}^2$.

178

179 *HR-XRD.*

180 Samples V126 and C11-14.5 were finely ground in an agate mortar for homogenization to
181 prepare powder samples for X-ray diffraction (XRD) experiments. For each sample,
182 approximately 20 mg was loaded into polyimide (Kapton) double capillaries (Microlumen,

183 Oldsmar, USA) 0.5 mm in diameter. The XRD data were collected using a 2-circle
184 diffractometer of the CRISTAL beamline at the SOLEIL synchrotron (Saint-Aubin, France) at
185 $\lambda = 0.7270 \text{ \AA}$, with an efficient Mythen 2 X 9K detector (Dectris, Switzerland) at 293 K. The
186 goniometer was calibrated, and the wavelength was refined using the LaB₆ standard (NIST,
187 SRM660a).

188 *EXAFS measurements and data processing*

189 XAFS experiments at the U L_{III} edge ($E(2p_{3/2}) = 17.166 \text{ keV}$) were performed at the INE-
190 Beamline (Rothe et al., 2012) of the Karlsruhe Research Accelerator (KARA, Karlsruhe,
191 Germany). The INE-Beamline is dedicated to the investigation of radionuclide materials with
192 hard X-ray spectroscopy techniques. The EXAFS spectra were recorded on bulk samples
193 conditioned as pellets with a diameter equal to 5 mm. The pellets were encapsulated by
194 double-containment sample holders and cooled near 115 K using a LN₂ cryostat (Oxford
195 Instruments OptistatDN) during data acquisition. Because of the low concentration of the
196 samples, EXAFS measurements were performed in fluorescence yield detection mode
197 averaging the U L _{α 1} fluorescence signal ($\sim 13.61 \text{ keV}$) recorded by a 4-element Vortex-ME4
198 SDD and a 1-element Vortex-60EX SDD (SIINT). The optics of the beamline comprises a
199 double-crystal monochromator (DCM), fitted with a pair of Ge<422> crystals for selection of
200 the required X-ray energy range, and a collimating and focusing mirror system (Rh-coated
201 silicon mirrors), applied for higher-harmonic rejection, vertical collimation and focusing of
202 the incident beam, respectively. The energy scale of the DCM was calibrated by assigning the
203 first inflection point of the Y K-edge XANES (obtained from an yttrium metal foil measured
204 in transmission mode) to the Y 1s-energy (17.038 keV). Spatially resolved XAFS
205 investigations were performed for petrographic thin section samples prepared by
206 impregnation of sample aggregates in epoxy resin of 30 mm thickness glued on a glass

207 substrate of 25 mm x 29 mm. Regions of interest were preselected from SEM images,
208 showing high contrast for U rich aggregates. These regions were relocated by means of a
209 visible light microscope aligned to the X-ray focus obtained by a polycapillary optic. A beam
210 spot size of $\sim 25\mu\text{m} \times 25\mu\text{m}$ on the thin section samples was achieved. The U $L_{\alpha 1}$ fluorescence
211 intensity was recorded by a 1-element Vortex-60EX SDD. Microfocus experiments were
212 conducted at room temperature.

213 *EXAFS data fitting*

214 Data processing was conducted using the ATHENA code (Ravel and Newville, 2005). The e_0
215 energy was identified at the maximum of the absorption edge for data fitting. Fourier
216 transformation (FT) in k^2 was performed between 3 and 12 \AA^{-1} with Hanning windows using
217 the ARTEMIS code (Ravel and Newville, 2005), except for the C11-14.5 thin section B
218 sample, which is very noisy, and FT had to be performed between 3 and 8 \AA^{-1} . Only one
219 global amplitude factor S_0^2 and one energy threshold correction factor ΔE_0 were used in all
220 paths. Phases and amplitudes were calculated using the FEFF6 simulation code (Rehr et al.,
221 2010) included in ARTEMIS and based on the modified structure of menasite (Plášil et al.,
222 2013), brannerite (Szymanski and Scott, 1982) and parsonsite (Locock et al., 2003) for uranyl
223 sulfates, uranium oxide, and uranyl phosphate, respectively. In addition, a modified model of
224 hydrogen uranyl phosphate tetrahydrate (Morosin, 1978), which has an equivalent structure to
225 chernikovite or ankoleite, has been used for a uranyl phosphate mineral. Single scattering
226 paths were considered for the oxygen, phosphorus, sulfur, iron or uranium atoms according to
227 the sample. Triple Oax-U-Oax scattering paths were also considered and linked to the
228 corresponding single paths for uranyl.

229

230 **Results**

231 *Uranium speciation in bulk samples*

232 XRD results with the diffractograms of V126 and C11-14.5 and the magnification of chosen
233 angular domains of interest are shown in ESI Fig. 1 and Figs. 2 a to c, respectively. The two
234 bulges at approximately 2.5 and 9.5 2θ on both diffractograms correspond to the Kapton
235 tubes. Quartz, K, and Na feldspar (orthoclase, microcline, albite) are detrital mineral heritages
236 of the Akouta sandstone formation. Phyllosilicates are kaolinite, the main component, illite,
237 smectite, interstratified chlorite/smectite, and palygorskite. Like hematite/goethite, anatase,
238 pyrite, and calcite, they are diagenetic signatures of sandstone formations. The only U(IV)
239 primary phase of the initial ore is uraninite, identified in the surficial crust (V126) with peaks
240 at 3.16 Å and 1.93 Å. Uranophane, the oxidized zone of the uranium deposit, is also identified
241 in the surficial crust (V126) with peaks at 7.91, 3.95, 3.61, and 2.99 Å. These minerals were
242 not identified in the paleolayer. Secondary minerals related to the U extraction process
243 (sulfuric acid) in these two samples are sulfates such as gypsum, natro-jarosite, plumbo-
244 jarosite, and jarosite. In the surficial crust sample, a higher variability of minerals is observed
245 with peculiar minerals not identified in the paleolayer: hydrated minerals such as
246 nordstrandite $\text{Al}(\text{OH})_3$, todorokite $(\text{Na,Ca,K})_2\text{Mn}_6\text{O}_{12}\cdot 3\text{-}4.5(\text{H}_2\text{O})$, quenstedtite
247 $\text{Fe}_2(\text{SO}_4)_3\cdot 10(\text{H}_2\text{O})$ and palygorskite $(\text{Mg,Al})_2\text{Si}_4\text{O}_{10}(\text{OH})\cdot 4(\text{H}_2\text{O})$ but also anhydrite (CaSO_4),
248 witnesses of the evaporation conditions. In addition, diffraction peaks of apatite
249 $(\text{Ca}_5(\text{PO}_4)_3(\text{Cl/F/OH}))$ are observed at 2.81 2.77 and 2.72 Å are observed in the surficial crust.
250 In the C11-14.5 diffractogram, vivianite occurrence $(\text{Fe}^{2+}_3(\text{PO}_4)_2 \cdot 8\text{H}_2\text{O})$ highlights different
251 conditions of diagenesis in the paleolayer.

252 The experimental EXAFS spectra of V126 and C11-14.5 at the U L_{III} edge are shown in Fig.
253 1 a, and the corresponding FT is presented in Fig. 1 b. The FTs are not corrected for the

254 EXAFS phase shift, so peaks appear at shorter distances ($R+\phi$) than the true near-neighbor
255 distances (R). The FT peaks below 1.5 Å are artifacts of spline removal and are not associated
256 with any coordination distance. For each sample, the modulus of the FT exhibits the
257 characteristic short-range axial shell of the two oxo bonds of UO_2^{2+} for the first coordination
258 sphere, of which the equatorial shell is also well resolved and indicates a single contribution.
259 A second coordination sphere is visible between $R+\phi = 2.2\text{-}3.3$ Å with a weaker signal and a
260 third between $R+\phi = 3.3\text{-}4.2$ Å for V126. The best fit metrical parameters are displayed in
261 Table 1. For the two samples, the two axial oxygen atoms are located at 1.78(1) Å. In the
262 equatorial uranyl plane, the U-O_{eq} distances are found at 2.37(1) Å for V126 and 2.41(1) Å
263 for C11-14.5. These distances are consistent with the number of equatorial oxygen atoms
264 fixed to 5 (Burns, 2005). The Debye-Waller factor associated with the contribution of the
265 equatorial oxygen atoms is rather high in both samples ($\sigma^2 = 0.0081$ Å² and $\sigma^2 = 0.0091$ Å² for
266 V126 and C11-14.5, respectively), indicating disorder in the second coordination shell. This
267 suggests that uranium is coordinated to small molecules such as H₂O, phosphates, or sulfates.
268 The different types of equatorial oxygen atoms were not distinguished in the fits to limit the
269 number of fitting parameters and because the k range was restricted to 3-12 Å⁻¹. A strong
270 contribution near 3.56 Å is systematically observed, corresponding to Oax-U-Oax multiple
271 scattering. The second coordination shell of uranium in V126 and C11-14.5 is composed of
272 sulfur contributions located at 3.10(2) Å and 3.17(3) Å, respectively, corresponding to
273 bidentate uranyl sulfates. The reported U...S distances for bidentate uranyl sulfates in the case
274 of EXAFS experiments on soluble complexes of uranyl sulfates are approximately 3.12 Å
275 (Moll et al., 2000; Hennig et al., 2008). This U...S distance can reach 3.17 Å in the case of
276 quantum chemical calculations on various isomers of $\text{UO}_2(\text{SO}_4)$ and $\text{UO}_2(\text{SO}_4)_2^{2-}$ (Vallet and
277 Grenthe, 2007). A second sulfur contribution at 3.62(3) Å for V126 and at 3.63(2) Å for C11-
278 14.5 completes the second coordination shell of uranium. This U...S distance is consistent

279 with those reported for monodentate uranyl sulfates (Moll et al., 2000; Hennig et al., 2008).
280 The coordination numbers of bi and monodentate sulfates in V126, equal to 0.8(2) and 0.8(3),
281 respectively, are lower than those in C11-14.5, equal to 2.1(3) and 1.2(2). This difference
282 could be related to the higher hydration rate in the crust (V126), which is more impacted by
283 hydration/evaporation cycles than the paleolayer (C11-14.5). The higher values of the Debye-
284 Waller factor associated with the second coordination shell of uranium in C11-14.5 can also
285 be explained by this difference in coordination numbers. An extra shell of uranium, composed
286 of 0.4(3) atoms at 3.94(4) Å, is also needed to increase the fit quality of V126. The addition of
287 the U-U contribution enhances the fit quality with an associated Rfactor and Qfactor equal to
288 1.3% and 5.34 respectively against 1.5% and 5.78 without the contribution. This weak
289 uranium contribution could correspond to the formation of uranyl oxyhydroxides, but residual
290 inherited uranophane, observed by HR-XRD, could not be excluded despite being a minor
291 component.

292

293 *Micromorphology, mineralogical and microgeochemical characterization of uranium phases*
294 *in V126 and C11-14.5*

295 Submicrometric mineralogical and chemical characterizations were performed on V126 and
296 C11-14.5 prepared as petrographic thin sections. Uranium-bearing minerals were identified by
297 SEM images (Fig. 2) combined with WDS microchemical analyses (Table 2) and mapping
298 (Fig. 3 and ESI Fig. 3). To further clarify, the space-resolved chemical analyses, numbered
299 one through thirteen, are marked by red stars, and the WDS maps are marked by red squares.
300 Each reported chemical composition is an average of five to ten measurements recorded
301 around red dots.

302 Inherited uranium phases from the initial ore were easily found in both the V126 and C11-
303 14.5 samples, most having sizes less than 5 μm . Nanometric to micrometric uranium-titanium
304 oxides are also dispersed in a chlorite/smectite matrix (Fig 2a). Submicrometric crystal
305 growth of uranium-titanium oxide on a montmorillonite pseudomorph occurred in fragmented
306 quartz (Fig 2b). These uranium-titanium oxides have homogeneous chemical compositions,
307 approximately 10 wt% Ti and ranging from 25.9 to 23.7 wt% U. (Table 2, areas 1 and 4). The
308 related U/Ti ratios are equal to 2.49 and 2.30, respectively, which is close to the 2.48 found
309 for brannerite (Willard et al., 1990). Iron (4.5 and 5.8 wt%), sulfur (1.8 and 2.8 wt%) and
310 molybdenum (2.5 and 2.0 wt%) were also detected. Fe and S are common impurities in
311 brannerite. The molybdenum is probably due to the presence of molybdenate relicts observed
312 in both samples.

313 A large altered uranium-molybdenate (>100 μm), composed of 35.0 wt% uranium and 25.9%
314 molybdenum, was observed in the V126 sample (Fig 2c, Table 2, area 6). The related U/Mo
315 ratio is equal to 1.35, a composition similar to moluranite, a hydrated U molybdenate found in
316 the environment, with a U/Mo ratio of 1.41 (Willard et al., 1990). Moluranite is a common
317 alteration product of brannerite that explains the ~2 wt % iron, sulfur and silicon
318 concentrations detected.

319 In the paleolayer (C11-14.5), a large uranium-rich zone (>300 μm) filled a quartz fissure (Fig.
320 2d). The WDS map shows a heterogeneous distribution of uranium ranging from 10 wt% to
321 65 wt % (Fig. 3). The richest uranium areas are composed of uranium oxide aggregates of a
322 few hundred nanometers (ESI Fig. 5). These nanometric uranium oxides (58.2 wt % mean
323 uranium) occur in a smectite-rich matrix (Table 2, area 7, ESI Fig. 3). Impurities such as 2.5
324 wt % Ti, 1.6 wt % Fe and 1.3 wt % P are also measured in the fissure. Rutile dispersed in the
325 fissure is observed. On the WDS maps, the iron and phosphorus concentrations display a

326 differential distribution. The central part of the fissure exhibits low concentrations of iron and
327 phosphorus (~2 wt % for both) and 60 wt% uranium. Conversely, higher concentrations of
328 iron and phosphorus are detected in the extremities of the fissure (~10 wt % of Fe and ~7 wt
329 % of P) and 10 wt % of uranium, suggesting a local alteration/dissolution process of these
330 inherited uranium oxides (Table 2, area 8)

331 Submicrometric cubic uranyl sulfate crystals growing on quartz within a kaolinite-rich
332 coating were identified in the crust (V126) (Fig. 2e). Microprobe analyses provide evidence
333 of iron sulfide as well in a background. A larger uranyl sulfate mineral or concretion of a few
334 tens of micrometers was also observed in this sample (Fig. 2f). The crystal composition is
335 23.1 wt % U and 4.4 wt % S (Table 2, area 9). The uranium concentration of the micrometric
336 uranyl sulfate mineral is higher than that of the small crystals (49.1 wt %), and the sulfur rate
337 is equivalent (Table 2, area 10). The U/S ratio of the crystals is equal to 5.25, whereas it is
338 equal to 10.9 for the mineral. The different micromorphologies and sizes suggest the
339 formation of two different phases of uranyl sulfates. The various sulfate neoformations in
340 both the surficial crust and paleolayer are related to extraction processes based on sulfuric
341 acid leaching.

342 Uranyl phosphates from a few tens to a few hundreds of micrometers were only found in the
343 paleolayer (Fig. 2 g and h). With a fan and sheet structure in the porosity of the tailings, they
344 are composed of 53.1 wt % uranium and 6.4 wt % phosphorus (Table 2, area 11). A large
345 uranyl phosphate coating (over 100 μm) with the same sheet structure and chemical
346 composition was also identified on a hydroxyapatite aggregate (Fig. 2 h, ESI Fig 4). The high
347 concentrations of phosphorus and calcium detected on the aggregate, 14.7 and 31.3 wt %,
348 respectively (Table 2, area 13), correspond to hydroxyapatite composition. The U/P ratio is
349 similar to the 7.6 value of uranyl phosphates, such as chernikovite or lermontovite. The

350 highest uranium concentration (55 wt%) occurs in the coating and fissure infillings of
351 hydroxyapatite. It should be noted that approximately 6 wt % uranium is detected in the
352 richest hydroxyapatite and central part of the aggregate. This value may be attributed to
353 dispersed submicrometric crystals of uranyl phosphates and eventually uranium sorption on
354 hydroxyapatite (Fuller et al., 2002). According to their occurrence, micromorphology and
355 sizes, these uranyl phosphate minerals are considered newly formed.

356 *μEXAFS characterizations of U-bearing minerals in C11-14.5*

357 EXAFS characterizations of both uranium oxide located in the crack fissures (Fig. 2d) and
358 uranyl phosphate coating growing on hydroxyapatite (Fig. 2 h) were performed at the U L_{III}
359 edge using a beam of 25μm x 25μm. These two minerals are located in the paleolayer (C11-
360 14.5). The sample was prepared as a petrographic thin section that allowed us to precisely
361 probe uranium speciation in these two minerals. The recorded EXAFS spectra are shown in
362 Fig. 1a, and the corresponding FT is presented in Fig. 1b. Despite an extended acquisition
363 time between 1 and 13 k and the merging of eight spectra, noise is important in these two
364 EXAFS spectra and forces us to fit until 11.5 k for uranyl phosphate and 8 k for uranium
365 oxide. The best fit metrical parameters are displayed in Table 1.

366 For uranium oxide, the modulus of the FT exhibits two strong contributions visible at $R+\phi =$
367 $1.5-2.5 \text{ \AA}$ and $R+\phi = 3.1-4 \text{ \AA}$, corresponding to the first and second coordination shells of
368 uranium (Fig. 1b). The shape and the $R+\phi$ of the first contribution confirm a U(IV) mineral.
369 The coordination shell of uranium is composed of 7.2(4) oxygen atoms at 2.37(1) \AA and
370 2.5(5) uranium atoms at 3.85(2) \AA , which is consistent with the U-O and U-U distances
371 reported for uraninite (Kelly, 2010). The weak contribution visible at $R+\phi = 2.5-3 \text{ \AA}$ can be
372 fitted with a U-O distance of 2.83(2) \AA , but this value is too long to be physically reasonable

373 for a uranium-oxygen bond length. The scattering contribution of this shell is assumed to be
374 mainly a contribution of silicon related to the mineral background of the fissure composed of
375 kaolinite. The coffinite USiO_4 contains a similar U-Si contribution reported to be 3.09 Å for
376 the SiO_4 polyhedron coordinated in a bidentate, edge-sharing fashion (Dreissig et al., 2011;
377 Fuchs and Gebert, 1958). The low Si concentration detected by WDS in this area (2.2 wt%,
378 Table 2, area 7) is not consistent with the Si concentration in coffinite (~7 wt%), which
379 excluded the possibility of coffinite occurrence (Willard et al., 1990).

380 Despite its low resolution, the FT modulus of uranyl phosphate (Fig 1b) exhibits the short-
381 range axial shell of the two oxo bonds of UO_2^{2+} . A shoulder associated with the first
382 contribution is also visible corresponding to the equatorial shell. The second and third
383 coordination spheres have a weaker signal and are located at $R+\phi = 2.2\text{-}3.3$ Å and $R+\phi = 3.5\text{-}$
384 4.1 Å, respectively. The first coordination shell is composed of two axial and five equatorial
385 oxygen atoms at 1.74(1) Å and 2.25(1) Å, respectively. A total of 1.7(7) phosphorus atoms at
386 3.55(3) Å from monodentate phosphate groups form the second coordination shell (Vazquez
387 et al., 2007; Kelly, 2010). The third coordination shell composed of 1.4(5) uranium atoms at
388 4.02(3) completes the coordination shell of uranium. The U-O_{eq} and U-P distances were
389 close to those reported for meta-autunite ($\text{Ca}(\text{UO}_2)_2(\text{PO}_4)_2 \cdot 6\text{H}_2\text{O}$) and meta ankoleite
390 ($\text{K}_2(\text{UO}_2)_2(\text{PO}_4)_2 \cdot 6\text{H}_2\text{O}$) (Thompson et al. 1997) but no calcium or potassium were detected
391 by WDS (Table 2). The identification of the uranyl phosphate phase based only on the
392 EXAFS data is difficult. Nevertheless, the reported U-P and U-U distances are similar to
393 those reported for uranyl orthophosphate (Catalano et al. 2004) and the presence of
394 hydroxyapatite could support the formation of uranyl orthophosphate (Locock et al. 2002). A
395 multiple scattering contribution, Oax-U-Oax, near 3.56 Å is also needed to fit the
396 experimental data. Together, the EXAFS and WDS results confirm the occurrence of uranyl
397 phosphate in the paleolayer.

398 **Discussion**

399 *Uranium speciation and paragenese*

400 EXAFS spectroscopy, HR-XRD, micromorphology, mineralogical and microgeochemical
401 characterization procedures were combined in this study to determine the mechanisms ruling
402 uranium mobility in the Cominak tailing pile. The selected samples V126 and C11-14.5 were
403 collected in the surficial crust and in a paleolayer (C11-14.5), a former surficial crust located
404 at 14.5 m depth, of the pile. The high U concentrations of these two environmental samples,
405 4100 ppm for V126 and 2250 ppm for C11-14,5, suggest a strong U reconcentration. EXAFS
406 spectroscopy performed on the bulk samples provided valuable data about dominant U
407 speciation in the samples. HR-XRD allowed us to describe the paragenesis and identify
408 uranium-bearing minerals. Micromorphology, microgeochemical analyses, and micro-EXAFS
409 spectroscopy performed on petrographic thin sections of the samples made possible the
410 characterizations of specific uranium phases, inherited or newly formed, and highlighted
411 mechanisms ruling the uranium immobilization.

412 The formation of uranyl (U^{VI}) groups was detected in the U-tailings samples by EXAFS
413 spectroscopy. In both samples, uranyl is mainly associated with sulfate groups (Table 1),
414 which is consistent with the chemical and environmental conditions occurring in the U-
415 tailings pile of Cominak. This pile is ruled by acidic pH and anthropic sulfur rich
416 environments. Oxidizing conditions and strong evaporation phenomena related to the
417 extremely arid Sahelian climate induce the neoformation of uranyl sulfates (Finch and
418 Murakami 1999). Various sulfate species were detected by HR-XRD in the samples, such as
419 gypsum $CaSO_4 \cdot 2H_2O$, natrojarosite $NaFe_3(SO_4)_2(OH)_6$, plumbojarosite $PbFe_3(SO_4)_2(OH)_6$
420 and quenstedtite $Fe_2(SO_4)_3 \cdot 11H_2O$. Sulfur contributions were identified in the coordination
421 shell of uranyl at 3.10 Å and 3.17 Å as well as 3.62 Å corresponding to bi and monodentate

422 uranyl sulfates (Moll et al., 2000; Vallet and Grenthe, 2007; Hennig et al., 2008).

423 Indications regarding the hydration rate can be deduced from the coordination numbers, equal
424 to 0.8 for bidentate and monodentate sulfur atoms in the surficial crust, while there are equal
425 to 2.1 and 1.2 for bidentate and monodentate sulfur atoms in the paleolayer. Among the five
426 oxygen atoms composing the equatorial shell of V126, 1.6 come from bidentate sulfates
427 (2x0.8) and 0.8 come from monodentate sulfates. The 2.6 remaining oxygen atoms
428 correspond to water molecules. In C11-14.5, the oxygen equatorial shell is composed of 4.2 O
429 from bidentate sulfates (2x2.1) and 1.2 from monodentate sulfates which confirm the absence
430 of water molecule in the coordination shell. Following this method, the equatorial shell would
431 be composed of 5.4 oxygen atoms. According to the estimated uncertainties, this value is
432 consistent with the value of this parameter in the fit fixed to 5. The average distance of the
433 oxygen equatorial shell also brings information about the composition of the coordination
434 shell. Considering the average distances of uranium-oxygen from monodentate sulfate (2.30-
435 2.37 Å), bidentate sulfate (2.42-2.48 Å) and waters molecules (2.41 Å) (Hennig et al., 2007),
436 it is possible to calculate theoretical distances of the oxygen equatorial shell. For V126 this
437 theoretical distance is equal to 2.41Å $((2.33 \times 0.8 O_{Sbid} + 2.45 \times 1.6 O_{Smon} +$
438 $2.41 \times 2.6 O_{water}) / 5 = 2.41)$ and for C11-14.5 to 2.42 Å $((2.33 \times 1.2 O_{Sbid} + 2.45 \times 4.2$
439 $O_{Smon}) / 5.4 = 2.42)$. For C11-14.5 the result is consistent with the EXAFS data but for V126
440 the result is higher of 0.04 Å. The presence of oxygen atoms from clay minerals in the
441 coordination shell of the uranyl, in addition to those from water molecules, could explain this
442 difference and indicate minor sorption phenomena on clay minerals. The higher hydration rate
443 of the surficial crust sample is related to the Sahelian climate. Minerals such as norstrandite in
444 the surficial sample and anhydrite confirm the variability of hydrometric occurrence at the
445 surface. The paleolayer located at 14.5 m depth is protected from surficial meteoric conditions
446 with more constant hydrometric conditions.

447 Uranyl sulfate minerals were only identified as micrometric cubic minerals or as
448 microconcretion in the surficial crust by SEM and WDS microprobe in petrographic thin
449 sections (Fig. 2e and 2f). They were not detected in the HR-XRD diffractograms. The
450 neoformation of uranyl sulfate minerals is therefore considered to be a minor process
451 compared to the formation of soluble forms of uranyl sulfate. The higher coordination number
452 associated with the sulfate groups in the paleolayer suggests the neoformation of uranyl
453 sulfate minerals. However, it was not observed in the paleolayer sample by SEM and WDS
454 microprobes.

455 In the surficial crust, relict primary uranium minerals were identified. Uranophane was
456 detected by HR-XRD as well as minor occurrence of uraninite (ESI Fig 2abc). Uranophane,
457 the U(VI) mineral resulting from the supergene alteration of uraninite, is more resistant to the
458 extraction process. Despite the high efficiency of the U-extraction process (95-98%),
459 uraninites resist the extraction process, especially when trapped in minerals such as quartz,
460 feldspar, or mica. A weak U-U contribution at 3.94 Å was identified by EXAFS spectroscopy
461 (Table 1). This U-U contribution is attributed to the formation of uranyl oxides certainly
462 formed from the oxidation of relict uranium primary minerals. Although a U-U contribution at
463 3.94 Å was reported for uranophane (Catalano et al 2004, Kelly, 2010), this U mineral is a
464 minor component of the V126 sample. Uranophane is rarely observed in tailings, and its
465 detection is related to the high sensitivity of HR-XRD for minor phases. In the bulk sample of
466 the paleolayer, no inherited uranium minerals were detected by EXAFS or HR-XRD, related
467 to the detection limits. Compared to the surficial layer, it suggests a reduced occurrence of
468 these minerals, probably due to time-related dissolutions according to the oxidizing conditions
469 in the pile.

470 Micromorphological in situ observations on petrographic thin sections highlight other residual
471 uranium phases in both samples, possibly minor for some of them. Submicrometric crystals of

472 brannerite, $((U,Ca,Ce)(Ti,Fe)_2O_6)$, are dispersed in a chlorite/smectite matrix aggregate with
473 relicts of K feldspars (Fig 2a) but also as nanometric spherules associated with montmorillonite
474 neoformations entrapped in a quartz crystal (Fig 2b). These oxides are refractory uranium
475 minerals of the ore and resist the U-extraction process (Lottering et al., 2008; Charalambous
476 et al., 2014). The clay minerals result from supergene alteration prior to the extraction
477 process. A uranium-molybdenum oxide such as moluranite was also observed in the V126
478 sample in a millimetric aggregate of quartz feldspar clay minerals with dispersed micrometric
479 pyrites, zircons, and galenas (Fig 2c). Moluranite, a U(IV)/U(VI) amorphous alteration
480 product of brannerite, formed when brannerite was highly altered by the extraction process.

481 A large U-rich zone located in a quartz fissure was identified in the paleolayer (Fig. 2d). U
482 concentration is approximately 58 wt%. Uranium(IV) was detected by space-resolved EXAFS
483 spectroscopy on a petrographic thin section. The number of uranium next neighbors equal to
484 2.5 is too low to be crystalline uraninite, which has 12 uranium next neighbors (Lander and
485 Mueller, 1974, Conradson et al., 2004). The low coordination number is a result of a strong
486 structural disorder possibly related to the nanometric size of the uranium (IV) oxide
487 aggregates (ESI Fig. 5). A weak single scattering contribution at 2.83(2) Å is attributed to
488 silicon atoms related to the smectite infilling observed in the fissure (ESI Fig. 3). This Si
489 contribution was described by Dreissig et al. during the formation of U(IV) colloids in the
490 presence of aqueous silicate solution. The U(IV) oxide and smectite overgrowths in such
491 fissures of quartz suggest inherited phases of supergene alteration prior to the U-extraction
492 process.

493 A heterogeneous distribution of uranium is observed in the fissure (Fig. 3) with U-
494 concentrations ranging from 35 wt% to 65 wt%, related to the growth of uranium(IV)
495 spherules on the smectite sheets in the closed part of the fissure. When no uranium(IV)
496 spherules are visible in the fissure, the smectite is 5 wt% U enriched. It could be attributed to

497 U sorption. In the open part of the fissure, the U concentration is approximately 10 wt%,
498 suggesting alteration of the uranium(IV) oxide concretions. In this zone affected by alteration
499 fluids, the mean concentrations of iron and phosphorus are 7 and 5 wt %, respectively. The
500 formation of iron oxides and phosphate groups refers to recent alteration conditions and
501 postextraction processes (Lahrouch et al., 2021). The colocalization of Fe and P observed on
502 the WDS map highlights a combination of iron oxide with phosphate groups that forms a trap
503 for uranium. This mechanism of uranium immobilization was already observed and described
504 in U-waste rock piles submitted to weathering (Lahrouch et al., 2021). In this open area
505 feature, the smectitic background is also another complementary trap of U immobilization.

506

507 Uranyl phosphate minerals were observed in the paleolayer as a few hundred micrometers
508 rosettes in the porosity of the samples (Fig. 2 g) or as coatings on hydroxyapatite (Fig. 2 h).
509 They are composed of ~55 wt % uranium and 7 wt % phosphorus (Table 2, area 7). The
510 uranyl coordination shell composed of monodentate phosphate groups and uranium is
511 consistent with the formation of uranyl orthophosphate (Catalano et al 2004, Locock et al.
512 2002). The uranyl groups are immobilized by uranyl phosphate mineral neoformations known
513 as insoluble phases. The P source for phosphates is the accessory mineral apatite observed by
514 SEM/WDS. Uranyl phosphate coatings on hydroxyapatite aggregates confirm the local
515 dissolution and reprecipitation of P. These uranyl orthophosphates may result from the
516 dissolution of apatite under acidic conditions controlled by Ca liberation (Dorozkhin, 1997).
517 These strong acidic conditions explain why more common autunite neoformations were not
518 observed (Kelly, 2010). Apatite is observed in the XR diffractogram of the surficial crust but
519 not in that of the paleolayer. This confirms a weak occurrence of this mineral in the
520 paleolayer and the in situ alteration/transformation of apatite in uranyl orthophosphate.
521 Another phosphate mineral, vivianite, a ferrous phosphate, suggests variable local redox

522 conditions, which is consistent with the conservation of relicts of uraninite in the global
523 oxidized facies.

524 The tailings pile is a hydrated sulfate-rich environment with gypsum, jarosite, and
525 quenstedtite (less than 2 wt% S). As described by EXAFS, uranyl is mainly associated with
526 sulfate groups, which are relative traps for uranium. Rare uranyl sulfate minerals were
527 observed by SEM/WDS, suggesting that neoformation is not the dominant process. The
528 surficial crust is submitted to cyclic evapotranspiration conditions of the Sahelian climate.
529 Local anhydrite occurrence in the surficial crust attests to a more arid period. These peaks of
530 evaporation favor the precipitation of uranyl sulfate minerals. In the paleolayer, the conditions
531 of hydration and temperature are more stable than in the surface. The uranyl groups are
532 associated with sulfate complexes, and the sulfate parageneses are similar to those in the
533 surficial crust except for quenstedtite. The neoformation of uranyl phosphate minerals
534 competes with uranyl sulfate minerals. The uranyl phosphate minerals precipitate according to
535 solubility constants (Gorman-Lewis et al., 2008) and possible pH modification. The P source
536 for these phosphate neoformations is the accessory mineral apatite from the Guezouman
537 sandstone, which also occurs in the surficial layer. The paleolayer, which is an ancient U-rich
538 surface of the tailings, evolves with time and confined medium to a globally more stable
539 environment for uranyl immobilization. Local reduced phases such as uraninite and vivianite
540 endure, but if redox conditions evolve, the vivianite alteration will possibly act as another
541 trap.

542

543 **Conclusions**

544 Uranium mobility in the two major U-enriched layers of the tailings pile of COMINAK was

545 studied at micrometric and molecular scales, the surficial crust and the 14.5 m deep paleolayer
 546 (an ancient surficial hard pan). The tailings were not neutralized with lime after the sulfuric
 547 acidic U extraction process. Acidic conditions control the uranyl speciation in the pile. Uranyl
 548 is mainly associated with the sulfate groups. Neof ormation of uranyl sulfates is favored by
 549 strong evapotranspiration phenomena due to Sahelian climates.

550 Uranyl phosphate occurrence in the deep paleolayer protected from surficial climatic
 551 conditions, suggesting that more stable hydration states and temperatures are efficient traps
 552 for uranium long-term mobility. The main source of P is apatite from the Guezouman
 553 sandstone dispersed in the tailings. In the paleolayer, local reduced conditions perdure with
 554 uraninite and vivianite occurrence. This other P source will possibly control the long-term
 555 mobility of uranium in case of modification of the redox conditions.

556

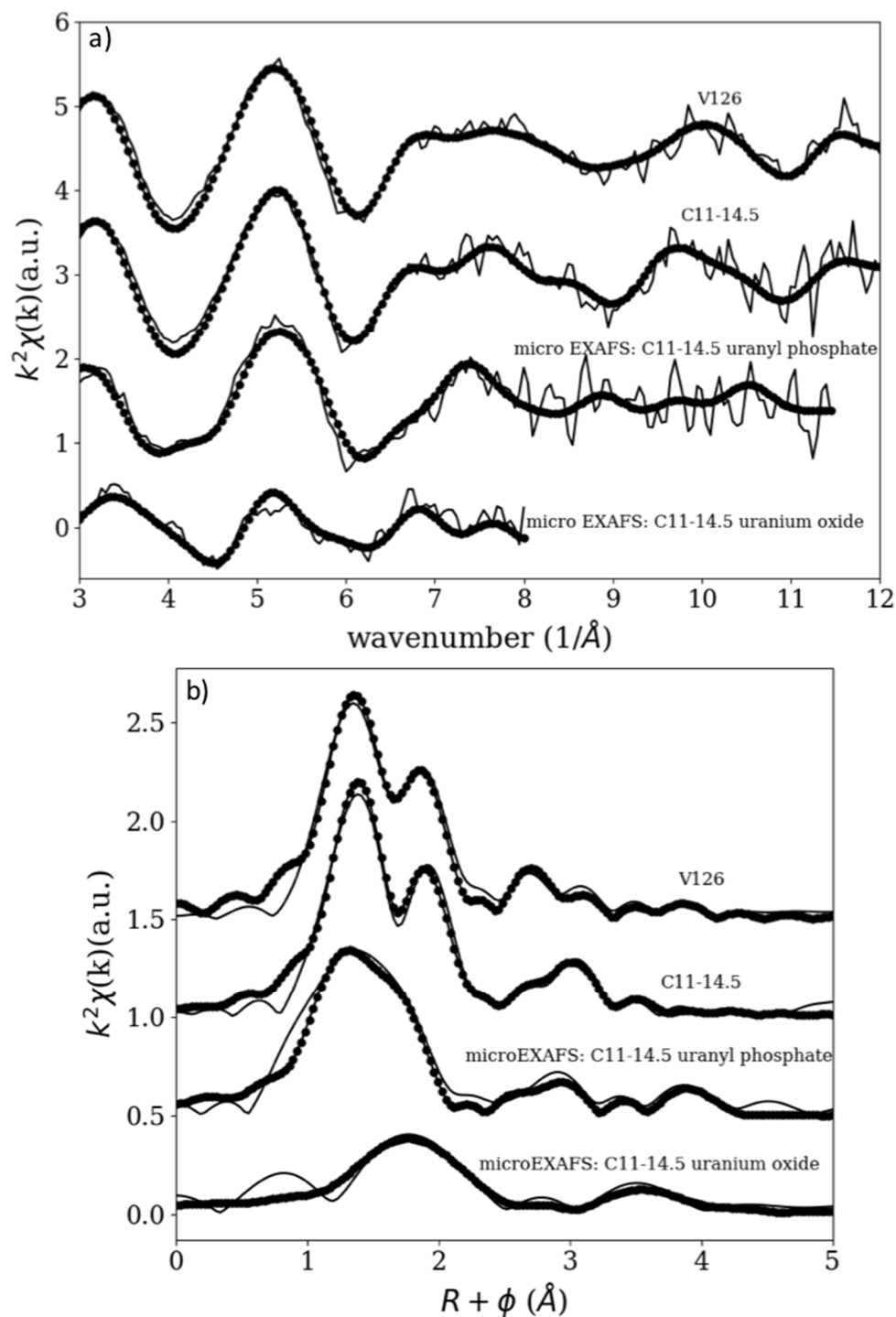
557 **Figures:**

558 Table 1: EXAFS best-fit parameters for V126, C11-14.5 (bulk samples) and for the micro
 559 EXAFS analyses of uranyl phosphate rosettes and uranium oxide minerals found in C11-14.
 560 CNs were fixed to 2 for the axial and 5 for the equatorial oxygen atoms in the case of uranyl
 561 configuration (numbers in italics). The numbers in parentheses are the estimated uncertainties,
 562 σ^2 is the Debye-Waller factor of the scattering path, S_0^2 is the global amplitude factor, e_0 is
 563 the energy threshold, R_{factor} is the quality factor of the fit in percent, and Q is the reduced χ_r^2
 564 factor of the fit.

	1 st coordination shell	2 nd coordination shell	Parameters
V126	2 O _{ax} at 1.78 (1) Å $\sigma^2 = 0.0026 \text{ \AA}^2$	0.8 (2) S _{bid} at 3.10 (2) Å $\sigma^2 = 0.0011 \text{ \AA}^2$	$S_0^2=1.0$ $e_0= -0.35 \text{ eV}$ $R_{\text{factor}}= 1.3\%$
	5 O _{eq} at 2.37 (1) Å	0.8 (3) S _{mon} at 3.62 (3) Å	

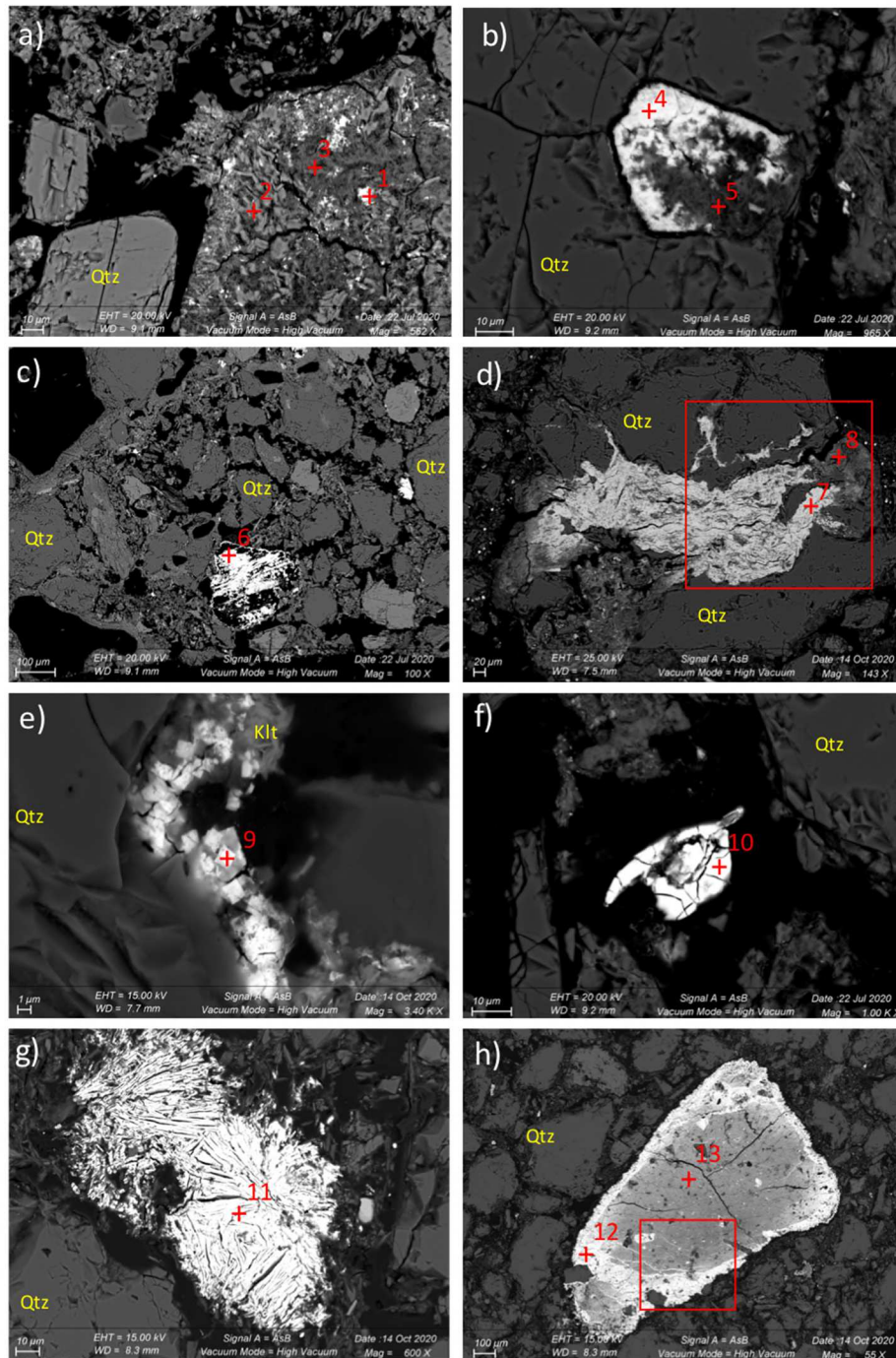
	$\sigma^2 = 0.0081 \text{ \AA}^2$	$\sigma^2 = 0.0015 \text{ \AA}^2$ 0.4 (3) U at 3.94 (4) \AA $\sigma^2 = 0.0032 \text{ \AA}^2$	Q= 5.34
C11-14.5	2 O _{ax} at 1.78 (1) \AA $\sigma^2 = 0.0021 \text{ \AA}^2$ 5 O _{eq} at 2.41 (1) \AA $\sigma^2 = 0.0091 \text{ \AA}^2$	2.1 (3) S _{bid} at 3.17 (3) \AA $\sigma^2 = 0.0115 \text{ \AA}^2$ 1.2 (2) S _{mon} at 3.63 (2) \AA $\sigma^2 = 0.0050 \text{ \AA}^2$	S ₀ ² =1.0 e ₀ = 2.65 eV R _{factor} = 1.5% Q= 1.39
Micro EXAFS: C11-14.5 uranyl phosphate	2 O _{ax} at 1.74 (1) \AA $\sigma^2 = 0.0059 \text{ \AA}^2$ 5 O _{eq} at 2.25 (1) \AA $\sigma^2 = 0.0077 \text{ \AA}^2$	1.7 (7) P at 3.55 (3) \AA $\sigma^2 = 0.0111 \text{ \AA}^2$ 1.4 (5) U at 4.02 (3) \AA $\sigma^2 = 0.0062 \text{ \AA}^2$	S ₀ ² =1.0 e ₀ = 1.48 eV R _{factor} = 2.0% Q= 2.08
Micro EXAFS: C11-14.5 uranium oxide	7.2 (4) O at 2.37 (1) \AA $\sigma^2 = 0.0240 \text{ \AA}^2$ 1.7 (3) O at 2.83 (2) \AA $\sigma^2 = 0.0045 \text{ \AA}^2$	2.7 (5) U at 3.85 (2) \AA $\sigma^2 = 0.0067 \text{ \AA}^2$	S ₀ ² =1.0 e ₀ = 2.10 eV R _{factor} = 2.5% Q= 3.71

565



566
 567 Figure 1: a) EXAFS spectra of V126, C11-14.5 recorded on the bulk samples and micro
 568 EXAFS spectra recorded on uranyl phosphate rosettes and uranium oxide minerals found in
 569 C11-14.5. b) Corresponding FT of the EXAFS spectra. Solid line = experimental spectrum.
 570 Dotted line = adjustment. Spectra are shifted in ordinates for clarity.

571



572

573 Figure 2: Back-scattering electron pictures of U-bearing minerals observed in petrographic
 574 thin sections of the crust (V126) and paleolayer (C11-14.5). a) Uranium-titanium oxides
 575 dispersed in a chlorite/smectite matrix (V126). c) A concretion of uranium-molybdenate
 576 (V126). b) Uranium-titanium oxide on a montmorillonite pseudomorph occurred in
 577 fragmented quartz (Qtz) (V126). d) A large uranium-rich zone filling a quartz fissure (C11-

578 14.5). e) Submicrometric cubic uranyl sulfate crystals growing on quartz within a kaolinite
579 (Klt)-rich coating (V126). f) A uranyl sulfate mineral or concretion (V126). g) A crystalized
580 uranyl phosphate(C11-14.5). h) A large uranyl phosphate coating on hydroxyapatite (C11-
581 14.5). The 1-9 red crosses correspond to WDS analyses (Table 2), and the red squares mark
582 the WDS maps.

583

584

585

586

587

588

589

590

591

592

593

594

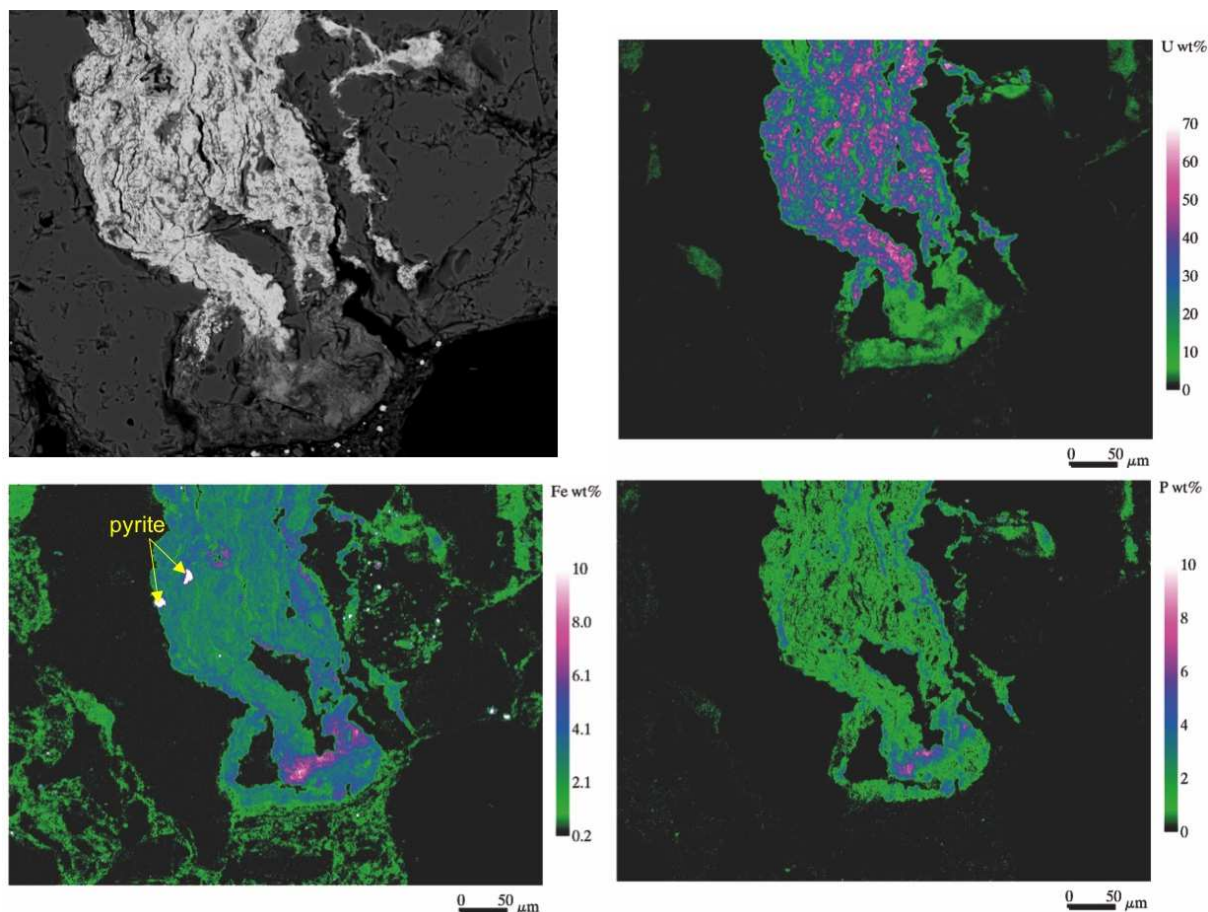
595

596 Table 2: WDS microchemical analyses recorded on V126 and C11-14.5 thin sections. Each
597 reported chemical composition (in wt %) is an average of five to ten measurements except for
598 2, 3 and 5. The values are presented with their standard deviations. The probed area (1 μ m
599 x1 μ m) is identified by red crosses (Fig. 2), numbered one through nine.

	Al	Si	K	Ca	Na	Fe	S	P	Mo	Ti	U	O*	total
1	2.71	7.88	0.31	0.51	0.47	5.84	2.76	0.79	2.04	10.32	23.72	30.39	92.35
	±	±	±	±	±	±	±	±	±	±	±	±	±
	0.38	1.73	0.11	0.08	0.13	2.11	0.23	0.09	0.21	1.05	3.48	1.38	0.73
2	15.96	25.32	7.00	0.14	0.18	2.23	0.56	0.15	0.00	0.05	0.13	47.38	101.59
	±	±	±	±	±	±	±	±	±	±	±	±	±
	nc	nc	nc	nc	nc	nc	nc	nc	nc	nc	nc	nc	nc
3	15.13	21.67	0.24	0.21	0.11	2.51	1.21	0.27	0.25	0.45	0.34	43.84	90.80
	±	±	±	±	±	±	±	±	±	±	±	±	±
	nc	nc	nc	nc	nc	nc	nc	nc	nc	nc	nc	nc	nc
4	2.57	4.89	0.28	0.34	0.21	4.49	1.80	0.53	2.49	10.44	25.95	24.95	82.04
	±	±	±	±	±	±	±	±	±	±	±	±	±
	0.52	1.73	0.31	0.13	0.06	0.14	0.52	0.03	0.22	0.25	1.22	2.49	4.18
5	9.56	20.92	0.86	0.07	0.17	2.18	2.84	0.27	0.51	0.85	2.02	38.76	81.26
	±	±	±	±	±	±	±	±	±	±	±	±	±
	nc	nc	nc	nc	nc	nc	nc	nc	nc	nc	nc	nc	nc
6	0.42	2.59	0.00	0.00	0.16	1.89	1.68	0.18	25.93	0.15	35.02	23.31	91.01
	±	±	±	±	±	±	±	±	±	±	±	±	±
	0.42	0.85	0.08	0.07	0.06	1.38	0.21	0.03	2.00	0.04	3.50	1.80	6.42
7	1.24	2.18	0.35	1.36	0.31	1.60	0.11	1.30	0.68	2.51	58.15	17.49	90.36
	±	±	±	±	±	±	±	±	±	±	±	±	±
	0.38	0.66	0.31	0.18	0.03	0.03	0.02	0.18	0.01	0.05	2.82	1.04	0.15
8	8.04	14.41	2.84	0.52	0.27	6.3	0.24	4.50	0.79	1.73	4.92	36.74	86.72
	±	±	±	±	±	±	±	±	±	±	±	±	±
	1.84	3.50	0.55	0.07	0.09	1.53	0.09	2.01	0.29	0.76	1.13	1.98	3.17
9	5.22	5.29	0.32	0.18	0.31	1.74	4.43	0.47	0.05	0.04	23.07	20.09	61.69
	±	±	±	±	±	±	±	±	±	±	±	±	±
	3.50	3.75	0.31	0.01	0.05	0.27	0.92	0.11	0.08	0.03	0.90	7.15	16.27
10	0.25	0.27	0.00	0.10	0.10	0.21	4.54	0.05	0.00	0.02	49.12	13.35	70.61
	±	±	±	±	±	±	±	±	±	±	±	±	±
	0.35	0.18	0.04	0.17	0.06	0.09	0.72	0.04	0.13	0.05	5.22	1.30	6.58
11	0.09	0.25	0.05	0.34	0.09	1.87	0.14	6.42	0.00	0.17	53.08	17.29	81.34
	±	±	±	±	±	±	±	±	±	±	±	±	±
	0.04	0.16	0.09	0.21	0.04	0.99	0.14	0.61	0.08	0.06	4.31	1.07	5.40
12	0.51	0.95	0.21	0.27	0.07	2.05	0.13	7.54	0.17	0.07	54.56	20.48	89.25
	±	±	±	±	±	±	±	±	±	±	±	±	±
	0.46	0.74	0.10	0.06	0.02	0.51	0.09	0.37	0.22	0.04	1.03	1.13	1.66
13	1.51	1.84	0.70	27.50	0.21	1.69	1.20	14.39	2.32	0.29	7.17	37.69	96.69
	±	±	±	±	±	±	±	±	±	±	±	±	±
	0.24	0.64	0.21	3.43	0.25	0.95	0.85	0.53	2.39	0.23	1.23	2.64	6.67

600

601



602

603 Figure 3: Back-scattering electron map of a portion of the C11-14.5 petrographic thin section
 604 with uranium oxides in a quartz fissure. Corresponding wavelength dispersive X-ray maps of
 605 uranium, iron and phosphorus. The scale is calculated in elementary mass percent (wt%). The
 606 white pixels correspond to the highest concentration, and the black pixels indicate the lowest.
 607 The pixel size is 1 μm x 1 μm .

608

609 **Declaration of competing interest**

610 The authors declare that they have no known competing financial interests or personal
 611 relationships that could have appeared to influence the work reported in this paper.

612

613 **Acknowledgments**

614 The authors acknowledge the KIT light source for provision of beamtime at the INE-
615 Beamline operated by the Institute for Nuclear Waste Disposal and would like to thank the
616 Institute for Beam Physics and Technology (IBPT) for the operation of the storage ring, the
617 Karlsruhe Research Accelerator (KARA).

618 In the framework of the CNRS RÉCIPROCS network, this work has been accepted for
619 synchrotron beamtime by the Soleil scientific proposal committee (BAG proposals
620 20191509). The authors would like to thank the SOLEIL Synchrotron Facility for use of
621 radiation facilities.

622 The authors also sincerely thank Omar Boudouma (Plateforme MEB-Sorbonne Université)
623 for acquisition of SEM images and Michel Fialin and Nicolas Rividi (CAMPARIS, IPGP,
624 Sorbonne Université) for wavelength-dispersive spectroscopy (WDS) measurements.

625 The authors thank ORANO Mining and COMINAK staff for their access to the samples. This
626 work was supported by ORANO Mining, Environmental R&D Department.

627

628 **References**

629

630 Abdelouas, A. (2006) Uranium mill tailings: geochemistry, mineralogy, and environmental
631 impact. *Elements*. 2, 335-341.

632 Angileri, A., Sardini, P., Donnard, J., Duval, S., Lefeuvre, H., Oger, T., Patrier, P., Rividi, N.,
633 Siitari-Kauppi, M., Toubon, H., Descostes, M. (2018) Mapping ²³⁸U decay chain
634 disequilibrium state in thin sections of geomaterials by digital autoradiography and
635 microprobe analysis. *Appl. Radiat. Isot.* 140, 228-237.

636 Ballini, M., Chautard, C., Nos, J., Phrommavanh, V., Beaucaire, C., Besançon, C., Boizard,
637 A., Cathelineau, M., Peiffert, C., Vercouter, T., Vors E., Descostes, M. (2020) A multi-
638 scalar study of the long-term reactivity of uranium mill tailings from Bellezane site
639 (France) *J. Environ. Radioact.* 106223.

640 Besançon, C., Chautard, C., Beaucaire, C., Savoye, S., Sardini, P., Gérard, M., Descostes, M.
641 (2020) The Role of Barite in the Post-Mining Stabilization of Radium-226: A Modeling
642 Contribution for Sequential Extractions. *Minerals*, 10, 497.

643 Boekhout, F., Gérard, M., Kanzari, A., Michel, A., Déjeant, A., Galois, L., Calas, G.,
644 Descostes, M., 2015. Uranium migration and retention during weathering of granitic
645 waste rock piles. *Appl. Geochem.* 58, 123-135.

646 Brugger, J., Burns, P.C., Meisser, N. (2003) Contribution to the mineralogy of acid drainage
647 of Uranium minerals: Marecottite and the zippeite-group. *Am. Mineral.* 88, 676-685.

648 Burns P.C. (2001) A new uranyl sulfate chain in the structure of uranopilite. *Canad. Mineral.*
649 39, 1139-1146.

650 Campbell, K.M., Veeramani, H., Ulrich, K.-U., Blue, L.Y., Giammar, D.E., Bernier- Latmani,
651 R., Stubbs, J.E., Suvorova, E., Yabusaki, S., Lezama-Pacheco, J.S., Mehta, A., Long,
652 P.E., Bargar, J.R., (2011). Oxidative dissolution of biogenic uraninite in groundwater at
653 Old Rifle, CO. *Environ. Sci. Technol.* 45, 8748-8754.

654 Carvalho, I. G., Cidu, R., Fanfani, L., Pitsch, H., Beaucaire, C., Zuddas, P. (2005) *Environ.*
655 *Sci. Technol.* 39, 8646-8652.

656 Catalano, J.G. and Brown Jr, G.E. (2004) Analysis of uranyl-bearing phases by EXAFS
657 spectroscopy: Interferences, multiple scattering, accuracy of structural parameters, and
658 spectral differences. *Am. Mineral.* 89, 1004-1021.

659 Cavellec, S. (2006) Evolution diagénétique du bassin de Tim Mersoï et conséquences pour la
660 genèse des minéralisations uranifères dans les formations carbonifères du Guezouman
661 et du Tarat (district Arlit-Akokan, Niger). Université Paris XI.

662 Charalambous, F.A., Ram, R., McMaster, S., Pownceby, M.I., Tardio, J., Bhargava, S.K.
663 (2014) Leaching behaviour of natural and heat-treated brannerite-containing uranium
664 ores in sulphate solutions with iron(III). *Miner. Eng.*, 57, 25-35.

665 Chautard, C., Beaucaire, C., Gerard, Phrommavanh, V., Nos, J., Galois, L., Calas, G., Roy,
666 R., Descostes. M. (2017) Geochemical characterization of U tailings (Bois Noirs
667 Limouzat, France). *Procedia Earth Planet. Sci.* 17, 308-311

668 Chautard, C., Beaucaire, C., Gerard, M., Roy, R., Savoye, S., Descostes. M. (2020)
669 Geochemical characterization of uranium mill tailings (Bois Noirs Limouzat, France)
670 highlighting the U and ²²⁶Ra retention. *J. Environ. Radioact.* 218, 106251.

671 Cox, J.D., Wagman, D.D., Medvedev, V.A. (1989) Codata key values for thermodynamics,
672 Hemisphere Publications, New York.

673 Cretaz, F., Szenknect, S., Clavier, N., Vitorge, P., Mesbah, A., Descostes, M., Poinssot C.,
674 Dacheux, N. (2013) Solubility properties of synthetic and natural meta-torbernite. *J.*
675 *Nucl. Mater.* 442, 195-207.

676 Déjeant, A., Bourva, L., Sia, R., Galois, L., Calas, G., Phrommavanh, V., Descostes. M.
677 (2014) Field analyses of ²³⁸U and ²²⁶Ra in two uranium mill tailings piles from Niger
678 using portable HPGe detector. *J. Environ. Radioact.* 137, 105-112.

679 Déjeant, A., Galois, L., Roy, R., Calas, G., Boekhout, F., Phrommavanh, V., Descostes, M.,
680 (2016) Evolution of uranium distribution and speciation in mill tailings, COMINAK
681 Mine, Niger. *Sci. Total Environ.* 545-546, 340-352

682 Denecke, M.A., Janssens, K., Proost, K., Rothe, J., Noseck, U. (2005) Confocal micrometer-
683 scale X-ray fluorescence and X-ray absorption fine structure studies of uranium

684 speciation in a tertiary sediment from a waste disposal natural analogue site. *Environ.*
685 *Sci. Technol.* 39, 2049-2058.

686 Dodo, A., Zuppi, G.M., (1999) Variabilité climatique durant le Quaternaire dans la nappe du
687 Tarat (Arlit, Niger). *C.R. Acad. Sci. Ser. IIA Earth Planet. Sci.* 328, 371–379.

688 Dorozhkin S. V. (1997) Surface reactions of apatite dissolution. *J. Colloid Interface Sci.* 191,
689 489- 497.

690 Dreissig, I., Weiss, S., Hennig, C., Bernhard, G., Zanker, H. (2011) Formation of
691 uranium(IV)-silica colloids at near-neutral pH. *Geochim. Cosmochim. Acta.* 75, 352–
692 367

693 Edwards, K. J., Bond, P. L., Druschel, G. K., McGuire, M. M., Hamers, R. J., Banfield, J. F.
694 (2000) Geochemical and biological aspects of sulfide mineral dissolution: lessons from
695 Iron Mountain, California. *Chem. Geol.* 169, 383-397.

696 Evangelou, V.P. and Zhang, Y.L. (1995) A review-pyrite oxidation mechanisms and acid
697 mine drainage prevention. *Crit. Rev. Environ. Sci. Technol.* 25, 141-199.

698 Felmy, A.R., Xia, Y., Wang, Z. (2005). The solubility product of $\text{NaUO}_2\text{PO}_4 \cdot x\text{H}_2\text{O}$
699 determined in phosphate and carbonate solutions. *Radiochim. Acta* 93, 401-408.

700 Fesenko, S., Carvalho, F., Martin, P., Moore, W.S., Yankovic, T. Radium in the Environment.
701 In *The Environmental Behaviour of Radium: Revised Edition*, IAEA: Vienna, Austria,
702 2014, 33-105.

703 Finch, R. and Murakami, T. (1999) Systematics and paragenesis of uranium minerals. In P.C.
704 Burns and R. Finch, Eds., *Uranium: mineralogy, geochemistry and the environment*, 38
705 *Reviews in Mineralogy*, Mineralogical Society of America, Washington, D.C. 91-179.

706 Forbes, P. (1989) Rôles des structures sédimentaires et tectoniques, du volcanisme alcalin
707 régional et des fluides diagenétiques - hydrothermaux pour la formation des
708 minéralisations à U-Zr-Zn-V-Mo d'Akouta (Niger). Université de Bourgogne

709 Fuller, C.C., Bargar, J. R., Davis, J. A., Piana, M. J. (2002) Mechanisms of uranium
710 interactions with hydroxyapatite: implications for groundwater remediation. *Environ.*
711 *Sci. Technol.* 36, 2, 158-165.

712 Fuchs, L.H. and Gebert, E. (1958) X-ray studies of synthetic coffinite, thorite, and uranorthite
713 *Am. Mineral.* 43, 243-248.

714 Gorman-Lewis, D., Burns, P.C., Fein, J.B. (2008) Review of uranyl mineral solubility
715 measurements. *J. Chem. Thermodynamics.* 40, 335-352.

716 Grenthe, I., Drozdzyński, J., Fujino, T., Buck, E. C., Albrecht-Schmitt T. E., Wolf. S. F.
717 Uranium. In “The Chemistry of the Actinide and Transactinide Elements”, 3rd ed.,
718 Edelstein, N. M., Fuger, J., Morss, L. R., Eds., Springer: Dordrecht, 2006, Vol. 1, Chap.
719 5, 253-698.

720 Grenthe, I., Fuger, J., Konings, R.J.M., Lemire, R.J., Muller, A.B., Nguyen-Trung Cregu, C.,
721 Wanner, H. (1992) Chemical thermodynamics of uranium. Elsevier, New York.

722 Grenthe, I., Lagerman, B. (1993) Ternary Metal Complexes. 2. The U(VI)-SO₂⁻⁴-OH⁻ System
723 *Radiochim. Acta.* 61, 169-176.

724 Hennig, C., Ikeda, A., Schmeide, K., Brendler, V., Moll, H., Tsushima, S., Scheinost, A. C.,
725 Skanthakumar, S., Wilson, R., Soderholm, L., Servaes, K., Görrler-Walrand, C., Van
726 Deun, R. (2008) The relationship of monodentate and bidentate coordinated
727 uranium(VI) sulfate in aqueous solution. *Radiochim. Acta.* 96, 607-611.

728 His, C.-K. D. and Langmuir, D. (1985) Adsorption of uranyl onto ferric oxyhydroxides:
729 application of the surface complexation site-binding model. *Geochim. Cosmochim.*
730 *Acta.* 49, 1931-1941.

731 Jamieson, H.E. (2011) Geochemistry and mineralogy of solid mine waste: essential
732 knowledge for predicting environmental impact. *Elements* 7, 381-386.

733 Jensen, K.A., Palenik, C.S., Ewing, R.C. (2002) U⁶⁺ phases in the weathering zone of the

734 Bangombé U-deposit: observed and predicted mineralogy. *Radiochim. Acta.* 90, 761-
735 769.

736 Jerden Jr, J.L. and Sinha, A.K. (2006) Geochemical coupling of uranium and phosphorous in
737 soils overlying an unmined uranium deposit: Coles Hill, Virginia. *J. Geochem. Explor.*
738 91, 56-70.

739 Jerden Jr., J.L. and Sinha, A.K. (2003) Phosphate based immobilization of uranium in an
740 oxidizing bedrock aquifer. *Appl. Geochem.* 18, 823-843.

741 Jerden Jr., J.L., Sinha, A.K., Zelazny, L., (2003) Natural immobilization of uranium by
742 phosphate mineralization in an oxidizing saprolite–soil profile: chemical weathering of
743 the Coles Hill uranium deposit, Virginia. *Chem. Geol.* 199, 129-157.

744 Jin, Q., Su, L., Montavon, G., Sun, Y., Chen, Z., Guo, Z., Wu, W. (2016) Surface
745 complexation modeling of U(VI) adsorption on granite at ambient/elevated temperature:
746 Experimental and XPS study. *Chem. Geol.* 433, 81-91.

747 Johnson D.B. and Hallberg K.B. (2005) Acid mine drainage remediation options: a review.
748 *Sci. Total Environ.* 338, 3-14.

749 Kelly, S.D. (2010) Chapter 14 - uranium chemistry in soils and sediments. *Dev. Soil. Sci.* 34,
750 411-466.

751 King, P. T., Michel, J., Moore, W. S. (1982) Ground water geochemistry of ²²⁸Ra, ²²⁶Ra
752 and ²²²Rn. *Geochim. Cosmochim. Acta* 46, 1173-1182.

753 Krivovichev, S. and Plàsil, J. (2013) Chapter 3: Mineralogy and crystallography of uranium.
754 In *Uranium Cradle to the Grave*. Mineralogical Association of Canada.

755 Lahrouch, F., Guo, N., Hunault, M. O. J. Y., Solari, P. L., Descostes, M., Gerard, M. (2021)
756 Uranium retention on iron oxyhydroxides in post-mining environmental conditions.
757 Chemosphere 128473.

758 Langmuir, D. (1978) Uranium solution-mineral equilibria at low temperatures with
759 applications to sedimentary ore deposits. *Geochim. Cosmochim. Acta.* 42, 547-569.

760 Lee, J.-K., Baik, M.-H., Choi, J.-W., Seo, M.-S. (2011) Development of a web-based sorption
761 database (KAERI-SDB) and application to the safety assessment of a radioactive waste
762 disposal. *Nucl. Eng. Des.* 241, 5316-5324.

763 Lin, J., Sun, W., Desmarais, J., Chen, N., Feng, R., Zhang, P., Li, D., Lieu, A., Tse, J. S.,
764 Pan.Y. (2018) Uptake and speciation of uranium in synthetic gypsum ($\text{CaSO}_4 \cdot 2\text{H}_2\text{O}$):
765 Applications to radioactive mine tailings. *J. Environ. Radioact.* 181, 8-17.

766 Locock, A. J., Burns, P. C., Flynn, T. M. (2005) The role of water in the structures of
767 synthetic hallimondite, $\text{Pb}_2[(\text{UO}_2)(\text{AsO}_4)_2](\text{H}_2\text{O})_n$ and synthetic parsonsite,
768 $\text{Pb}_2[(\text{UO}_2)(\text{PO}_4)_2](\text{H}_2\text{O})_n$, $0 < n < 0.5$. *Am. Mineral.* 90, 240-246.

769 Lottering, M.J., Lorenzen, L., Phala, N.S., Smit, J.T., Schalkwyk G.A.C., (2008) Mineralogy
770 and uranium leaching response of low grade South African ores. *Miner. Eng.* 1, 16-22.

771 Martin, G.R., Tuck, D.G., (1959) The specific activity of radium. *Int. J. Appl. Radiat. Isot.* 5,
772 141-145.

773 Molinari, J., Snodgrass, W.J. The Chemistry and Radiochemistry of Radium and the Other
774 Elements of the Uranium and Thorium Natural Decay Series. In The Environmental
775 Behaviour of Radium, IAEA Technical ^[L]_[SEP]Report Series No. 310, IAEA: Vienna,
776 Austria, 1990, Volume 1, pp.11–56. ISBN 92-0-125090-8.

777 Moll, H., Reich, T., Hennig, C., Rossberg, A., Szabó, Z., Grenthe, I. (2000) Solution
778 coordination chemistry of uranium in the binary UO_2^{2+} - SO_4^{2-} and the ternary UO_2^{2+} -
779 SO_4^{2-} - OH^- system. *Radiochim. Acta* 88, 559-566

780 Morin, G. and Calas, G. (2006) Arsenic in soils, mine tailings, and former industrial sites.
781 *Elements*, 2, 97-101.

- 782 Morosin, B. (1978). Hydrogen uranyl phosphate tetrahydrate, a hydrogen ion solid electrolyte.
783 *Acta Crystallogr. Sect. B.* 34, 3732-3734.
- 784 Murakami, T., Ohnuki, T., Isobe, H., Sato, T. (1997) Mobility of uranium during weathering.
785 *Am. Mineral.* 82, 888-899.
- 786 Murakami, T., Sato, T., Ohnuki, T., Isobe, H. (2005) Field evidence for uranium
787 nanocrystallization and its implications for uranium transport. *Chem. Geol.* 221, 117-
788 126.
- 789 Nirdosh, I., Muthuswami, S.V., Baird, M.H.I. (1984) Radium in uranium mill tailing – Some
790 observations on retention and removal. *Hydrometallurgy*, 12, 151-176.
- 791 Pagel, M., Cavellec, S., Forbes, P., Gerbaud, O., Vergely, P., Wagani, I., Mathieu, M. (2005)
792 Uranium deposits in the Arlit area (Niger). *Mineral Deposit Research: Meeting the*
793 *Global Challenge*, 303-305.
- 794 Park, I., Tabelin, C. B., Jeon, S., Li, X., Seno, K., Ito, M., Hiroyosh, N. (2019) A review of
795 recent strategies for acid mine drainage prevention and mine tailings recycling.
796 *Chemosphere* 219, 588-606.
- 797 Payne, T. E., Davis, J. A., Waite, T. D. (1996) Uranium Adsorption on Ferrihydrite - Effects
798 of Phosphate and Humic Acid. *Radiochim. Acta.* 74, 239-243.
- 799 Plášil, J., Kampf, A. R., Kasatkin, A. V., Marty, J., Škoda, R., Silva, S., Čejka, J. (2013)
800 Meisserite, $\text{Na}_5(\text{UO}_2)(\text{SO}_4)_3(\text{SO}_3\text{OH})(\text{H}_2\text{O})$, a new uranyl sulfate mineral from the Blue
801 Lizard mine, San Juan County, Utah, USA. *Mineral. Mag.* 77, 2975-2988.
- 802 Rai, D., Xia, Y., Rao, L., Hess, N.J., Felmy, A.R., Moore, D.A., McCready, D.E. (2005)
803 Solubility of $(\text{UO}_2)_3(\text{PO}_4)_2 \cdot 4\text{H}_2\text{O}$ in $\text{H}^+ - \text{Na}^+ - \text{OH}^- - \text{H}_2\text{PO}_4^- - \text{HPO}_4^{2-} - \text{PO}_4^{3-} - \text{H}_2\text{O}$ and
804 its comparison to the analogous PuO^{2+}_2 system. *J. Solut. Chem.* 34, 469-498.
- 805 Ravel, B., Newville, M. (2005) IUCr ATHENA, ARTEMIS, HEPHAESTUS: data analysis
806 for X-ray absorption spectroscopy using IFEFFIT, *J. Synchrotron Radiat.* 12, 537-541.

807 Rehr, J. J., Kas, J. J., Vila, F. Prange D. M. P., Jorissen, K. (2010) Parameter-free calculations
808 of X-ray spectra with FEFF9, *Phys. Chem. Chem. Phys.* 12, 5503-5513.

809 Rothe, J.; Butorin, S.; Dardenne, K.; Denecke, M.A.; Kienzler, B.; Löble, M.; Metz, V.;
810 Seibert, A.; Steppert, M.; Vitova, T.; Walther, C.; Geckeis, H. (2012) The INE-
811 beamline for actinide science at ANKA. *Rev. Sci. Instrum.* 83, 043105.

812 Schindler, M., Durocher, J. L., Kotzer, T. G., Hawthorne, F.C. (2012) Uranium-bearing
813 phases in a U-mill disposal site in Northern Canada: Products of the interaction between
814 leachate/raffinate and tailings material. *Appl. Geochem.* 29, 151-161.

815 Sharifironizi, M. and Burns, P. C. (2018) Investigation of the structural stability of zippeite-
816 group minerals using high-temperature calorimetry. *Canad. Mineral.* 56, 7-14.

817 Shock, E.L., Sassani, D.C., Betz, H. (1997) Uranium in geologic fluids - estimates of standard
818 partial molal properties, oxidation potentials, and hydrolysis constants at high
819 temperatures and pressures *Geochim. Cosmochim. Acta*, 61, 4245-4266.

820 Singh, A., Ulrich, K.-U., Giammar, D.E. (2010). Impact of phosphate on U(VI)
821 immobilization in the presence of goethite. *Geochim. Cosmochim. Acta.* 74, 6324-6343.

822 Sowder, A.G., Clark, S.B., Fjeld, R.A. (2001) The impact of mineralogy in the U(VI)-Ca-
823 PO₄ system on the environmental availability of uranium. *J. Radioanal. Nucl. Chem.*
824 248, 517-524.

825 Steinhausler, F. and Zaitseva, L. (2007) Uranium mining and milling: material security and
826 risk assessment. *Int. J. Nucl. Govern. Econ. Ecol.* 1, 286-304.

827 Szymanski, J. T. and Scott J. D. (1982) A crystal-structure refinement of synthetic brannerite,
828 U₂Ti₂O₆, and its bearing on rate of alkaline-carbonate leaching of brannerite in ore.
829 *Canad. Mineral.* 20, 271-279.

830 Thompson, H.A., Brown, G.E, Parks, G. A. (1997) XAFS spectroscopic study of uranyl
831 coordination in solids and aqueous solution. *Am. Mineral.* 82, 483-496.

- 832 Vazquez, G.J., Dodge, C.J., Francis, A.J. (2007) Interactions of uranium with polyphosphate.
833 *Chemosphere* 70, 263-269.
- 834 Wellman, D.M., (2006) Effects of pH, temperature, and aqueous organic material on the
835 dissolution kinetics of meta-autunite minerals, $(\text{Na,Ca})_2\text{-1}[(\text{UO}_2)(\text{PO}_4)]_2 \cdot 3\text{H}_2\text{O}$. *Am.*
836 *Mineral.* 91, 143-158.
- 837 Wellman, D.M., McNamara, B.K., Bacon, D.H., Cordova, E.A., Ermi, R.M., Top, L.M.
838 (2009). Dissolution kinetics of meta-torbernite under circum-neutral to alkaline
839 conditions. *Environ. Chem.* 6, 551-560.
- 840 Willard R. L., Campbell, T. J., Rapp, G. R. (1990) Encyclopedia of Minerals, 2nd ed. New
841 York: Van Nostrand Reinhold, London: Chapman & Hall.
- 842

